American Society of Hematology
2021 L Street NW, Suite 900,
Washington, DC 20036
Phone: 202-776-0544 | Fax 202-776-0545
editorial@hematology.org

Evolution of tumor subclones and T-cell dynamics underlie variable ibrutinib responses in Waldenström macroglobulinemia

Tracking no: BLD-2025-032268R2

Hao Sun (Dana-Farber Cancer Institute, United States) Romanos Sklavenitis Pistofidis (Department of Medical Oncology, Dana-Farber Cancer Institute, Boston, MA, USA, United States) Shirong Liu (Dana Farber Cancer Institute, United States) Xia Liu (Dana-Farber Cancer Institute, United States) Nickolas Tsakmaklis (Dana Farber Cancer Institute, United States) John Hatcher (Dana-Farber Cancer Institute, United States) Maria Luisa Guerrera (Dana Farber Cancer Institute, United States) Amanda Kofides (Dana Farber Cancer Institute, United States) Andres Ramirez-Gamero (Bing Center for Waldenström Macroglobulinemia, Dana-Farber Cancer Institute, Boston, MA, USA,) Abigail Peachey (Dana-Farber Cancer Institute, United States) Shuqiang Li (Dana-Farber Cancer Institute, United States) Derin Keskin (DFCI HArvard, United States) Vipheaviny Chea (Dana-Farber Cancer Institute, United States) Nawoo Kim (Dana-Farber Cancer Institute, United States) Haoxiang Lyu (Dana-Farber Cancer Institute, United States) Wesley Lu (Dana-Farber Cancer Institute, United States) Kenneth Livak (Dana-Farber Cancer Institute, United States) Kirsten Meid (Dana Farber Cancer Institute, United States) Alberto Guijosa (Dana Farber Cancer-Institute, United States) Catherine Flynn (Dana Farber Cancer Institute, United States) Dominic Pizzarella (Dana-Farber Cancer Institute, United States) Christopher Patterson (Dana-Farber Cancer Institute, United States) Mu Hao (Blood hospital and hematology institute, state key lab of experimental hematology, China) Shuhua Yi (Institute of Hematology and Blood Disease Hospital, Chinese Academy of Medical Sciences and Peking, China) Weiping Yuan (State Key Laboratory of Experimental Hematology, National Clinical Research Center for Blood Diseases, Haihe Laboratory of Cell Ecosystem, Institute of Hematology & Blood Diseases Hospital, Chinese Academy of Medical Sciences & Peking Union Medical College, China) Andrew Branagan (Massachusetts General Hospital, United States) Catherine Wu (Dana-Farber Cancer Institute, Harvard Medical School, United States) Irene Ghobrial (Dana-Farber Cancer Institute, United States) Lugui Qiu (State Key Laboratory of Experimental Hematology, National Clinical Research Center for Hematological Disorders, Institute of Hematology and Blood Diseases Hospital, Chinese Academy of Medical Sciences, China) Shayna Sarosiek (Dana Farber Cancer Institute, United States) Jorge Castillo (Dana-Farber Cancer Institute, United States) Zachary Hunter (Dana Farber Cancer Institute, United States) Steven Treon (Dana Farber Cancer Institute, United States)

Abstract:

To elucidate the molecular basis underlying differential response and resistance to ibrutinib in Waldenström's macroglobulinemia (WM), we conducted a prospective phase II trial (ClinicalTrials.gov; NCT02604511) of ibrutinib monotherapy in treatment-naïve patients. Seventy-four sequential bone marrow (BM) aspirates from 17 patients, collected from baseline through 48 treatment cycles, were profiled using single-cell multi-omics. BM cells segregated primarily into B/plasma cell and T-cell compartments. Longitudinal clonal tracking of malignant B/plasma cells identified three distinct evolutionary patterns: "evolution" (early clone contraction with late clone expansion and increasing genomic complexity), "devolution" (early clone expansion with late clone contraction and genomic simplification), and "no-evolution" (stable clonal architecture). The "evolution" pattern was strongly associated with disease progression, whereas "devolution" correlated with durable clinical response. Transcriptomic profiling of resistant clones enabled development and validation of the Waldenström's Ibrutinib Prediction (WIP) score, which predicted treatment response at baseline. Within the WIP signature, LYN emerged as a key regulator; LYN knockdown or inhibition significantly increased WM cell sensitivity to ibrutinib, suggesting a rational combinatorial strategy. In parallel, GZMB^{+} CD8^{+} effector-memory (TEM) cells expanded post-treatment in progressing patients and co-existed with tumor "evolution". These cells exhibited persistently impaired cytotoxic programs (e.g., GNLY), a de-differentiated memory-like state, elevated PDCD1 expression, and reduced TCR diversity. Together, this study provides the first single-cell framework of tumor clonal evolution and T-cell dysfunction under ibrutinib in WM; introduces the WIP score as a predictive biomarker for treatment response; and identifies actionable tumor-intrinsic and immune mechanisms driving resistance.

Conflict of interest: COI declared - see note

COI notes: SPT received research funding, and/or consulting fees from Abbvie/Pharmacyclics Inc., Janssen Oncology Inc., Beigene Inc., Eli Lilly Pharmaceuticals, Bristol Myers Squibb, and Ono Pharmaceuticals. JJC received research funds or consulting fees from Abbvie, AstraZeneca, Avilar, BeOne, Cellectar, Johnson & Johnson, LOXO, and Pharmacyclics. SRS received research funding and/or consulting fees from ADC Therapeutics, Beigene, Cellectar, and SOBI. DBK serves as a scientific advisor for Immunitrack (a wholly owned subsidiary of Eli Lilly and Company) and Breakbio, and holds equity in Affimed N.V., Agenus, Armata Pharmaceuticals, Breakbio, BioMarin Pharmaceutical, Celldex Therapeutics, Editas Medicine, ImmunityBio, Lexicon Pharmaceuticals, Moderna, Sana Biotechnology, and Summit Therapeutics. JMH received consulting fees from Arbella Therapeutics. RSP is a co-founder, equity holder and consultant in PreDICTA Biosciences. The remaining authors declare no competing financial interests.

Preprint server: No;

Author contributions and disclosures: SPT conceived and designed the study. SPT, RSP, and SRL supervised the study and provided conceptual guidance. HS performed the research and conducted the bioinformatic analyses. SRL and SQL performed single-cell multi-omic library preparation and sequencing. HS, XL, SRL, NT, MLG, AK, ALP, and DP processed samples and carried out laboratory experiments. JMH conducted drug synthesis and enzymatic inhibition assays. HS analyzed and interpreted the experimental data. NT, ARG, AG, CAF, CJP, KM, ARB, SRS, JJC, and SPT identified and collected clinical samples and/or analyzed clinical data. SQL, DBK, VC, NK, HL, WL, KJL, and KM provided valuable insights into sample sequencing. RSP, ARB, CJW, IMG, LGQ, SHY, WPY, MH, SRL, ZRH, and SPT provided scientific insights and guidance on data analysis and interpretation. HS and RSP drafted the initial manuscript, and all authors critically revised the paper for important intellectual content.

Non-author contributions and disclosures: No;

Agreement to Share Publication-Related Data and Data Sharing Statement: Raw single-cell RNA, BCR, and TCR-seq data analyzed in this study will be shared on EGA (study sites pending).

Clinical trial registration information (if any): NCT02604511

Evolution of tumor subclones and T-cell dynamics underlie variable ibrutinib responses in Waldenström macroglobulinemia

Hao Sun,[1-4*] Romanos Sklavenitis-Pistofidis,[2,3,5*] Shirong Liu,[1-3,*] Xia Liu,[1-3] Nicholas Tsakmaklis,[1-3] John M. Hatcher,[1-3] Maria Luisa Guerrera,[1-3] Amanda Kofides,[1-3] Andres Ramirez-Gamero,[1,3] Abigail L. Peachey,[1-3] Shuqiang Li,[2,3,6] Derin B. Keskin,[2,3,5-8] Vipheaviny Chea,[2,3,6] Nawoo Kim,[2,3,6] Haoxiang Lyu,[2,3,6] Wesley Lu,[2,3,6] Kenneth J. Livak,[2,3,6] Kirsten Meid,[1,3] Alberto Guijosa,[1,3] Catherine A. Flynn,[1,3] Dominic Pizzarella,[1-3] Christopher J. Patterson,[1-3] Mu Hao,[4] Shuhua Yi,[4] Weiping Yuan,[4] Andrew R. Branagan,[3,9] Catherine J. Wu,[2,3,6] Irene M. Ghobrial,[2,3] Lugui Qiu,[4] Shayna R. Sarosiek,[1,3] Jorge J. Castillo,[1,3] Zachary R. Hunter,[1-3] Steven P. Treon.[1-3]

[1] Bing Center for Waldenström Macroglobulinemia, Dana-Farber Cancer Institute, Boston, MA, USA.

[2] Department of Medical Oncology, Dana-Farber Cancer Institute, Boston, MA, USA.

[3] Harvard Medical School, Boston, MA, USA.

[4] State Key Laboratory of Experimental Hematology, National Clinical Research Center for Blood Diseases, Haihe Laboratory of Cell Ecosystem, Institute of Hematology & Blood Diseases Hospital, Chinese Academy of Medical Sciences & Peking Union Medical College, Tianjin, China.

[5] Broad Institute of MIT and Harvard, Cambridge, MA, USA.

[6] Translational Immunogenomics Laboratory, Dana-Farber Cancer Institute, Boston, MA, USA.

[7] Department of Computer Science, Metropolitan College, Boston University, Boston, MA, USA.

[8] Section for Bioinformatics, Department of Health Technology, Technical University of Denmark, Lyngby, Denmark.

[9] Massachusetts General Hospital Cancer Center, Boston, MA, USA.

[*] These authors contributed equally to this work.

Corresponding author:
Steven P. Treon, M.D., Ph.D.
Bing Center for Waldenström's Macroglobulinemia
Dana Farber Cancer Institute
450 Brookline Avenue, Boston, MA 02215 USA
Tel: (617) 632-2681 Fax: (617) 632-4862
Email: steven_treon@dfci.harvard.edu

Short Title: Single-cell insights into variable ibrutinib responses

Text Word Count: 3988/4000

Abstract Word Count: 241/250

Figures and Tables: 6/7

References: 69/100

Keywords: Single-cell multi-omics, ibrutinib, genomic evolution, response predictor, resistance, immune dysfunction, GZMB⁺ CD8⁺ TEM cells

Supplemental Tables: 6

Supplemental Figures: 8

Scientific category: Lymphoid Neoplasia

Data sharing statement: The single-cell RNA, BCR, and TCR sequencing data generated in this study have been deposited in the European Genome-phenome Archive (EGA; https://ega-archive.org/)

under accession number EGAS50000001596.

Key Points

- Three distinct evolutionary patterns of tumor subclone are associated with variable ibrutinib response and predicted by the WIP score.

- Expanded GZMB$^+$ CD8$^+$ TEM cells exhibit CD27$^+$ TCF1$^+$ de-differentiated features and impaired cytotoxicity in non-responders after treatment.

Abstract

To elucidate the molecular basis underlying differential response and resistance to ibrutinib in Waldenström’s macroglobulinemia (WM), we conducted a prospective phase II trial (ClinicalTrials.gov; NCT02604511) of ibrutinib monotherapy in treatment-naïve patients. Seventy-four sequential bone marrow (BM) aspirates from 17 patients, collected from baseline through 48 treatment cycles, were profiled using single-cell multi-omics. BM cells segregated primarily into B/plasma cell and T-cell compartments. Longitudinal clonal tracking of malignant B/plasma cells identified three distinct evolutionary patterns: “evolution” (early clone contraction with late clone expansion and increasing genomic complexity), “devolution” (early clone expansion with late clone contraction and genomic simplification), and “no-evolution” (stable clonal architecture). The “evolution” pattern was strongly associated with disease progression, whereas “devolution” correlated with durable clinical response. Transcriptomic profiling of resistant clones enabled development and validation of the Waldenström’s Ibrutinib Prediction (WIP) score, which predicted treatment response at baseline. Within the WIP signature, LYN emerged as a key regulator; *LYN* knockdown or inhibition significantly increased WM cell sensitivity to ibrutinib, suggesting a rational combinatorial strategy. In parallel, GZMB$^+$ CD8$^+$ effector-memory (TEM) cells expanded post-treatment in progressing patients and co-existed with tumor “evolution”. These cells exhibited persistently impaired cytotoxic programs (e.g., *GNLY*), a de-differentiated memory-like state, elevated *PDCD1* expression, and reduced TCR diversity. Together, this study provides the first single-cell framework of tumor clonal evolution and T-cell dysfunction under ibrutinib in WM; introduces the WIP score as a predictive biomarker for treatment response; and identifies actionable tumor-intrinsic and immune mechanisms driving resistance.

Introduction

Waldenström macroglobulinemia (WM) is a rare indolent B-cell lymphoma characterized by bone marrow (BM) infiltration with lymphoplasmacytic cells and secretion of monoclonal IgM.[1] More than 95% of WM patients harbor *MYD88* mutations that activate Bruton's tyrosine kinase (BTK), establishing ibrutinib as the first FDA- and EMA-approved BTK inhibitor for WM.[2-4] While some patients derive durable remission from ibrutinib, a substantial fraction relapse early.[4-7] Two clinical challenges remain: identifying patients unlikely to benefit from ibrutinib before treatment, and defining the molecular and immunologic drivers of relapse.

Across B-cell malignancies, resistance to targeted therapy is increasingly understood as an evolutionary process shaped by therapeutic selection. Ibrutinib can favor the outgrowth of pre-existing or emergent subclones through on-target alterations in BTK signaling and downstream effectors,[8-10] as well as broader programs involving tumor suppressor pathways and genomic instability.[11-13] In WM, baseline genetic features, including CXCR4 mutations[14-16] and high-risk lesions such as TP53 abnormalities and del(6q)[11,17,18], have been linked to inferior depth and durability of response to ibrutinib. However, most prior studies relied on bulk profiling, which masks intratumoral heterogeneity and obscures how competing tumor subclones adapt under sustained BTK inhibition.[19-21]

From an evolutionary perspective, WM tumors, particularly as revealed by single-cell profiling,[22,23] consist of heterogeneous, co-existing malignant subclones. Ibrutinib imposes a selective bottleneck, favoring adaptive subclones while suppressing others. However, how these clonal dynamics evolve over time in patients—and how they shape the immune microenvironment—remains poorly defined. Notably, despite evidence that BTK inhibition alters T-cell states,[24,25] longitudinal data on T-cell functional dynamics are limited.

To address these gaps, we conducted a prospective phase II trial of ibrutinib monotherapy in WM, incorporating longitudinal multi-omics profiling of serial BM samples.[26] Using paired single-cell RNA sequencing (scRNA-seq), B-cell receptor sequencing (scBCR-seq), and T-cell receptor sequencing (scTCR-seq), we analyzed 74 samples with a median 5-year follow-up, generating the largest single-cell dataset in WM. This enabled direct longitudinal tracking of malignant subclones and immune cell states. Within this evolutionary framework, we showed that WM patients followed distinct clonal evolutionary patterns under ibrutinib, reflecting alternative adaptive responses to therapy. These patterns were associated with differences in baseline tumor architecture, subsequent genomic remodeling, and immune dysfunction. By integrating tumor and T-cell dynamics, we developed and validated a baseline transcriptomic predictor of resistance, the Waldenström Ibrutinib Prediction (WIP) score, identified mechanisms underlying clonal adaptation, and uncovered progressive remodeling of CD8$^+$ effector-memory T cells (TEM) during tumor evolution. Together, our findings positioned response to ibrutinib in WM as the product of tumor–immune co-evolution and provided a framework for predicting treatment outcome and guiding rational therapeutic strategies.

Methods

Study design and sample collection

A prospective, investigator-initiated phase II trial of ibrutinib monotherapy was conducted in treatment-naïve WM (ClinicalTrials.gov NCT02604511).[26] BM aspirates were collected at baseline and during therapy (cycles 6–48).

Data processing and analysis

Single-cell data were processed with Cell Ranger (v7.0.0)[27] and Scanpy (v1.9.6)[28]. Clonotypes were reconstructed with Cell Ranger vdj,[27] and integrated using scirpy (v0.22.0)[29]. Tumor clonotypes were determined based on expanded BCRs, while subclonal phylogenies were inferred with Numbat (v1.3.2_1).[30]

Molecular and cellular profiling

Differentially expressed genes (DEGs) were assessed with two-sided Wilcoxon tests at the single-cell level and PyDESeq2 (v0.4.9) at the pseudo-bulk level.[31] Pathway analyses were conducted using Ingenuity Pathway Analysis (IPA)[32] and GSEApy (v1.1.0)[33]. Subclone composition was modeled using scCODA (v0.1.9) to define evolutionary patterns.[34]

Detailed protocols are provided in the **Supplementary Methods**.

Results

Single-cell multi-omic profiling of BM tumor and immune cells under ibrutinib monotherapy in patients with WM

To elucidate determinants of ibrutinib response and resistance within malignant and immune compartments, we analyzed sequential BM aspirates from WM patients enrolled in a prospective phase II study of Ibrutinib monotherapy.[26] A total of 74 longitudinal samples from 17 patients were collected at baseline and cycles 6 (6mo), 12 (1y), 24 (2y), 36 (3y), and 48 (4y) (**Suppl. Table 1**). These samples underwent 5′ scRNA-seq, complemented with paired scBCR-seq to determine malignancy (**Fig. 1A**). Treatment responses were assessed according to the modified criteria of the 6th International Workshop on WM.[35] Patients achieving partial response (PR) or better were responders (n = 11), while those with minimal response (MR), stable disease (SD), or progressive disease were non-responders (n = 6). In total, we obtained 634,414 high-quality cells for downstream analysis, including a large B/plasma cell population (n = 148,458) and normal immune cells (n = 485,956), such as T cells, NK cells, and myeloid cells (**Fig. 1B**). As the majority of cells detected were either B/plasma cells or T cells, we focused downstream analyses on these populations.

Within the B/plasma cell compartment, malignant and normal subsets were identified using the matched scBCR-seq data and normal cells were further stratified into pre-B cells, memory B cells, and plasma cells (**Fig. 1C**). Malignant B cells exhibited patient-specific clustering, whereas malignant plasma cells aggregated into a single cluster (n = 5,235), largely contributed by patients W012 and W015 (**Suppl. Fig. 1A, B**). Malignant B cells were further stratified into memory B cell–like (MBC-like) and plasma cell–like states based on established markers,[23] and WM patient subtypes were defined according to the dominant cell state (**Suppl. Fig. 1C–E**). No significant association was observed between these WM subtypes and clinical response to ibrutinib (**Suppl. Table 2**). As expected, responders exhibited a sustained decrease in tumor cell proportion, whereas non-responders showed fluctuating or increasing tumor cell levels (**Suppl. Fig. 1F**).

In the T cell compartment (n=286,077), we identified CD4$^+$ and CD8$^+$ naïve (TN) and central memory T (TCM) cells, regulatory T cells (Tregs), GZMK$^+$ CD4$^+$ T cells, GZMB$^+$ CD4$^+$ T cells, CD8$^+$ effector memory (TEM) subsets characterized by either high *GZMK* or high *GZMB* expression (the latter subdivided by KIR gene expression), γδ T cells (Tgd), mucosal-associated invariant T (MAIT) cells, metallothionein-high T cells (MT$^+$ T), and interferon stimulation gene-expressing (IFN$^+$) T cells (**Fig. 1D**).

Distinct evolutionary patterns in malignant B cells associated with response to ibrutinib in patients with WM

To characterize clonal dynamics during ibrutinib monotherapy, we inferred copy number variants (CNVs) in malignant cells using Numbat[30] (**Suppl. Fig. 2A**) and reconstructed phylogenetic trees in 13 patients; no CNVs were detected in four patients.

In patient W010, malignant cells comprised a dominant tumor with three subclones (**Fig. 2A**): clone 1 lacked CNVs, clone 2 acquired amp(6p) and del(6q), and clone 3 acquired an additional del(20) (**Fig. 2B**). Transcriptomic clustering paralleled CNV-based subclones, and pseudotime analysis outlined a trajectory from pre-B to memory B cells with sequential emergence of clones 1–3. (**Fig. 2A**). Longitudinal tracking revealed early clone 1 dominated at baseline, whereas late clone 3 expanded after six cycles of ibrutinib and persisted through cycles 12–48 (**Fig. 2C**). This patient harbored truncating CXCR4 p.T318fs and an ARID1A frameshift deletion at both baseline and post-treatment. In addition, TBK1 p.E355K and TBK1 p.G356K emerged following treatment (**Suppl. Fig. 2B**). This pattern, contraction of early tumor subclones and expansion of genomically complex late subclones post-therapy, was termed “evolution”. In total, we identified “evolution” in 4/13 patients (31%, 95% CI: 10-61) (**Fig. 2G**).

In contrast, patient W003 exhibited the opposite pattern. Phylogenetic reconstruction identified four subclones: clone 1 (earliest, no CNV), clone 2 (del(6q)), clone 3 (additional del(7q)), and clone 4 (latest, additional amp(4q)) (**Fig. 2D, E**). Pseudotime analysis revealed stepwise differentiation from clone 1 to clone 4, with malignant plasma cells enriched at the terminal differentiation (**Fig. 2D**). Clone 4 dominated at baseline but contracted after treatment, while clone 1 expanded and persisted. This patient harbored nonsense mutations in ARID1A and UBE2G1 at baseline, both of which were no longer detectable post-treatment (**Suppl. Fig. 2B**) and achieved a durable PR (**Fig. 2F**). We termed this “devolution”, defined by enrichment of early clones and reduction of late tumor clones under ibrutinib, resulting in decreased genomic complexity. Devolution occurred in 6/13 patients (46%, 95% CI: 20-74%) (**Fig. 2G**).

A third pattern, termed “no-evolution”, occurred in 3/13 patients (23%, 95% CI: 6-54%), characterized by stable clonal proportions and minimal CNV alterations during treatment. A representative patient is visualized in **Suppl. Fig. 3A–C**.

Notably, transcriptomic pseudotime consistently correlated with genomic evolution across the 13 patients with detectable CNVs. Clonal assignments based on CNVs also showed strong concordance with transcriptomic clusters within each patient (two-sided Spearman's r=0.68, P<1e-16) (**Suppl. Fig. 3D, E**), supporting the use of transcriptomic clusters as a surrogate for clonal mode classification. Accordingly, in the four patients without CNVs, transcriptomic clusters were used to infer evolutionary patterns: three "devolution" and one "no-evolution".

Integrating all 17 patients, the distribution of clonal evolutionary patterns differed significantly between ibrutinib responders and non-responders. In three of four "evolution" patients, major clonal shifts were detected 6–24 months before clinical progression (**Fig. 2G**). Among responders, the majority displayed "devolution" (81.8%), whereas none of the non-responders exhibited "devolution". In contrast, "evolution" was observed exclusively in non-responders (66.7%) (**Suppl. Table 3**; two-sided Fisher's exact test, P=0.00097). The association remained significant when limited to CNV-based analyses (**Suppl. Table 4**).

Consistent with these patterns, "evolution" patients showed an initial decrease followed by a rebound increase in CNV burden after treatment, whereas "no-evolution" and "devolution" patients exhibited sustained or fluctuating decreases (**Suppl. Fig. 3F**). Gain-of-function CXCR4 mutations, including p.S338*, p.S342*, and p.T318fs, were detected in 75% of "evolution" patients, significantly higher than "devolution" (22%) and "no-evolution" (25%) (two-sided Fisher's exact test, P=0.038) (**Suppl. Fig. 2B**). del(6q) tended to be more prevalent in "evolution" patients (75%) than in other groups (**Suppl. Fig. 2A**).

Transcriptomic signature of resistant clones predicts response to ibrutinib at diagnosis

We next sought transcriptional predictors of response and resistance to ibrutinib. Because resistant subclones may represent only a minor fraction at baseline, we performed subclone-aware differential expression (SADE) analysis, comparing resistant clones (expanded post-treatment) and sensitive clones (contracted during therapy) within the same tumor at baseline across the four "evolution" patients who progressed.

We identified 130 genes consistently dysregulated in resistant clones (93 upregulated, 37 downregulated) across all four patients (**Suppl. Fig. 4A, B**). Functional enrichment grouped these genes into ten clusters (**Fig. 3A**). A "response to unfolded protein" cluster (e.g., *HSPA5, HSP90B1, CALR, XBP1*) was downregulated in resistant clones, whereas multiple clusters were upregulated, including "antigen processing and presentation" (e.g., *HLA-DRB5, CD74*), "E3 ubiquitin ligase complex" (e.g., *CUL4A, CTNNB1*), and "B-cell receptor signaling" (e.g., *LYN, SYK, PRKCB, DOCK8*) (**Fig. 3B**).

We ranked genes by an integrated importance score combining fold change and network connectivity, identifying 30 high-importance genes (>0.6; 17 upregulated, 13 downregulated; **Fig. 3C**). From this set, we derived a Waldenström's Ibrutinib Prediction (WIP) score and validated it in an independent bulk RNA-seq dataset from 47 WM patients treated with ibrutinib monotherapy (excluding derivation cases). Patients with high baseline WIP scores had a significantly greater risk of disease progression than those with low scores (two-sided, log-rank P=0.013) (**Fig. 3D**).

Targeting WIP gene *LYN* overcomes ibrutinib resistance

To functionally validate the WIP signature and evaluate its therapeutic relevance, we focused on *LYN*, the top-ranked WIP gene by importance score (**Fig. 3C**). Short-hairpin–mediated *LYN* knockdown in WM cell lines (BCWM.1 and MWCL-1) reduced phosphorylation of BCR-downstream kinases, including p-STAT3, p-AKT, p-SYK, and p-ERK, while inducing compensatory p-IκBα, most prominently in MWCL-1 (**Fig. 3E**). Moreover, we observed significantly enhanced sensitivity to ibrutinib, as well as increased apoptosis post-ibrutinib in WM cell lines with *LYN* knockdown (**Fig. 3F and Suppl. Fig. 4C-3E**).

To test whether LYN inhibition can overcome resistance to ibrutinib, we generated ibrutinib-resistant WM cell lines via gradual dose escalation (**Fig. 3G, H**). Ibrutinib-resistant WM cell lines exhibited elevated *LYN* expression by qPCR (**Fig. 3I**). We then evaluated a covalent BTK/LYN dual inhibitor,[36] which displayed potent inhibition of BTK and LYN kinase activities (IC_{50}<0.6 nM; **Suppl. Fig. 4F, G**). The dual inhibitor increased cytotoxicity and apoptosis in WM cell lines, particularly in resistant cells, effectively overcoming ibrutinib resistance (**Fig. 3J and Suppl. Fig. 4H, I**).

Immunoblotting confirmed that ibrutinib-resistant cell lines expressed higher levels of LYN protein and maintained BTK phosphorylation despite ibrutinib exposure, whereas the BTK/LYN dual inhibitor suppressed phosphorylation of both kinases (**Fig. 3K**). Together, these results indicate that the WIP signature captures actionable dependencies and dual BTK/LYN inhibition may benefit patients with high WIP score who are less likely to respond to ibrutinib alone.

Divergent usage of gene programs post-therapy between resistant and sensitive clones in patients with WM

To characterize transcriptional remodeling induced by ibrutinib, we compared post-treatment and baseline gene expression separately for early and late tumor clones within each patient and evaluated pathway activities using IPA. We analyzed results by evolutionary pattern (“evolution”, “devolution”, or “no-evolution”) and identified 27 pathways altered in ≥75% of patients within each group.

In “evolution” patients (n = 4), late tumor clones showed upregulation of PD-L1, inflammatory, and interferon-γ signaling after treatment, whereas early clones showed little change (**Fig. 4A and Suppl. Fig. 5A**). BCR signaling was suppressed more strongly in early than late clones, while oxidative phosphorylation followed a biphasic pattern—initially increasing, then declining with continued therapy.

In contrast, an inverse pattern was observed in tumor cells from “devolution” patients, with late clones exhibiting greater reductions in interferon, MYC, NF-κB, and BCR signaling compared with early clones (**Suppl. Fig. 5B, 6A**). In line with their clonal equilibrium, we observed no consistent upregulation of signaling pathways after treatment in “no-evolution” patients (**Suppl. Fig. 6B**).

In “evolution” patients, hypoxia signaling progressively increased in late resistant clones across treatment cycles but decreased in early sensitive clones (**Fig. 4B**). Moreover, six of the hypoxia-associated genes—*HIF1A*, *DUSP1*, *MAP3K1*, *CXCR4*, *CDKN1A*, and *BTG1*—were consistently upregulated in late tumor clones after ibrutinib (**Fig. 4C and Suppl. Fig. 7A–7F**). Compared with memory B cells from healthy donors (HDs; n = 13), WM cells from treatment-naïve patients (n = 266) expressed significantly lower *HIF1A* (**Suppl. Fig. 7H**). Notably, in two of four patients, late resistant clones already exhibited significantly higher HIF1A expression at baseline than normal memory B cells (**Suppl. Fig. 7I**). To validate this observation in our cell line models, we performed immunofluorescence and flow cytometry experiments and demonstrated that resistant WM cell lines express higher levels of HIF-1α protein at baseline compared to sensitive lines, and this difference is further enhanced following ibrutinib treatment (**Fig. 4D, E and Suppl. Fig. 6G**). Collectively, the data suggest that a subset of WM resistant clones has elevated baseline *HIF1A* and that ibrutinib preferentially selects for *HIF1A*-high cells. These findings implicate hypoxia signaling as a contributor to ibrutinib resistance and provide mechanistic insight into pathways underlying response and relapse.

Exclusively expanded GZMB$^+$ CD8$^+$ TEM cells in "evolution" patients exhibit de-differentiation into dysfunctional CD27$^+$ TCF7$^+$ memory-like T cells

Seeing that clonal evolution underlay progression post-treatment with ibrutinib, we hypothesized that T cell clonal dynamics may also change in relation to tumor evolution and therapeutic pressure. Using scTCR-seq across all samples, we identified T cell clones based on shared TCR sequences, which were further classified as small, medium, or large based on their relative abundance within each sample, representing increasing degrees of clonal expansion. Consistent with prior reports,[37] clonal expansion occurred predominantly within cytotoxic effector-memory T cells (**Fig. 5A**). Longitudinal analysis of TCR diversity, quantified by the Chao1 index—a richness-based estimator in which lower values indicate reduced diversity and increased clonal dominance—revealed a significant decrease in diversity following ibrutinib treatment in "evolution" patients, indicating enhanced T cell clonal expansion. In contrast, patients with "devolution" and "no-evolution" patterns exhibited a significant increase in TCR diversity over time (**Fig. 5B**). Moreover, large T cell clones (>10% of the TCR repertoire per sample) were significantly overrepresented in "evolution" patients compared with the other groups (Fisher's exact test, $P = 0.012$) (**Fig. 5C**). Together, these findings indicate that pronounced T cell clonal expansion accompanies tumor clonal evolution and may reflect T cell dysfunction or ineffective tumor clearance.

To explore how T cell clonal expansion is associated with T cell functionality, we next analyzed the phenotype of clonally expanded T cells. We observed that large T cell clones were primarily of the GZMB$^+$ CD8$^+$ TEM cell (KIR$^+$ or KIR$^-$) phenotype and originated from small clones present at baseline, while Tregs remained exclusively within small clones and showed no evidence of expansion post-therapy (**Fig. 5D**). Additionally, GZMB$^+$ CD8$^+$ TEM cells (KIR$^+$ or KIR$^-$) expanded significantly in proportion in "evolution" patients after ibrutinib therapy, but remained stable or declined in other patterns (**Fig. 5E and Suppl. Fig. 8A, B**). Interestingly, T cells from large clones exhibited significantly reduced cytotoxic scores compared to their non-expanded counterparts within each patient (**Fig. 5F**). Differential expression analysis further revealed that within GZMB$^+$ CD8$^+$ TEM cells, large expanded T cells across post-treatment timepoints expressed lower levels of multiple cytotoxic effector genes, including *NKG7*, *GNLY*, and *PRF1*, compared with non-expanded T cells (**Fig. 5G**). Notably, however, they expressed higher levels of *CD27*, *IL7R*, and *TCF7*, indicating a de-differentiated, memory-like phenotype. At the cohort level, cytotoxic scores of GZMB$^+$ CD8$^+$ TEM cells remained consistently higher in “devolution” patients compared to both “evolution” and “no-evolution” patients, suggesting that T cell cytotoxicity scores may play a role in tumor evolution (**Fig. 5H**).

Comparative transcriptomic analysis showed that, relative to “devolution”, GZMB$^+$ CD8$^+$ TEM cells in “evolution” patients upregulated *BCL2*, *UBASH3B*, *SIRPG*, *CD27*, and *TCF7*, while downregulating *GNLY*, *CD247*, *TXK*, *TNFRSF18*, *FCER1G*, *S100A4*, and *IGFBP7*. The expression pattern in “no-evolution” patients largely resembled that of “evolution” patients (**Fig. 5I and Suppl. Fig. 8C**). Pathway enrichment analysis revealed reduced interferon signaling alongside increased hypoxia, CXCR4 signaling, and TNF-α signaling (**Suppl. Fig. 8D**). In patients belonging to the “evolution” group, *HIF1A* expression showed an increasing trend following ibrutinib therapy (paired Wilcoxon test, $P = 0.127$; **Suppl. Fig. 8E**).

Baseline transcriptional features of GZMB$^+$ CD8$^+$ TEM cells predict various response to ibrutinib

Given the pronounced differences in expansion dynamics and transcriptional programs of GZMB$^+$ CD8$^+$ TEM cells across clonal evolutionary patterns after ibrutinib, we next examined whether their baseline expression signatures were associated with treatment outcomes. At diagnosis, GZMB$^+$ CD8$^+$ TEM cells from non-responders versus responders displayed 58 differentially expressed genes (**Suppl. Table 6**). Downregulated genes in non-responders included *GNLY*, *CD247*, *CD226*, *S100A4*, *S100A6*, *SERPINB1*, *TXK*, and *BOK*, whereas upregulated genes included *LGALS9*, *CDK6*, *STK10*, *TNFSF9*, and *TGFBR3* (**Fig. 6A, B**). Among these, *GNLY* expression was significantly lower in non-responders, with strong discriminatory power between responders and non-responders (AUC = 0.91; **Fig. 6C**).

Based on these differential genes, we derived a non-responder GZMB$^+$ CD8$^+$ TEM score, which was significantly higher in non-responders compared to responders (**Fig. 6C**). Importantly, integration with tumor-intrinsic features revealed that baseline WIP scores of malignant cells were negatively correlated with *GNLY* expression in GZMB$^+$ CD8$^+$ TEM cells, and positively correlated with the non-responder GZMB$^+$ CD8$^+$ TEM score (**Fig. 6D**). Single-cell BM profiles from six age-matched HDs, processed using the same workflow as WM patient samples, served as normal controls for GZMB$^+$ CD8$^+$ TEM cells (**Suppl. Fig. 8F, G**). Overall, HDs exhibited intermediate expression levels of the non-responder TEM gene set compared with responders and non-responders (**Fig. 6E**). Specifically, *GNLY* expression in responders was comparable to that in HDs, whereas it was significantly downregulated in non-responders. Consistently, the non-responder TEM score was lower in responders than in HDs but markedly elevated in non-responders relative to HDs (**Fig. 6F**). Analysis of T cell exhaustion–associated genes demonstrated significantly elevated *PDCD1* expression in GZMB$^+$ CD8$^+$ TEM cells from WM patients relative to HDs (**Fig. 6G and Suppl. Fig. 8H**). Moreover, *PDCD1* expression was highest in “evolution” patients compared with the other two evolutionary groups (**Fig. 6H**).

Finally, we delineated the dynamic co-evolution of tumor and T-cell compartments in progressing patients under ibrutinib (**Fig. 6I**). Tumor cells exhibited an “evolution” pattern of clonal architecture, with early CNV-negative clone contracting after therapy, while genomically complex late clones—characterized by upregulated *LYN* expression at baseline and induction of HIF-1α under treatment—emerged as dominant. Concurrently, T cells in these patients showed declining TCR diversity after therapy. Baseline GZMB$^+$ CD8$^+$ TEM cells exhibited reduced *GNLY* expression and elevated *PDCD1* levels. Following treatment, these cells expanded proportionally yet maintained low cytotoxicity, acquired hypoxia signaling, and adopted a de-differentiated CD27$^+$ TCF7$^+$ memory-like phenotype.

Discussion

The introduction of BTK inhibitors, including ibrutinib, has markedly improved outcomes across multiple B-cell malignancies, including WM.[38-40] Nevertheless, resistance and relapse remain major clinical challenges.[41-43] Conceptually, escape from BTK inhibition can arise through several non–mutually exclusive routes: (i) reactivation of BCR/BTK pathway signaling via on-target or proximal signaling alterations,[8,44-46] (ii) adaptive bypass and pro-survival rewiring that reduces BTK dependence,[47-53] and (iii) a permissive genomic context, often reflected by cytogenetic lesions or tumor suppressor disruption.[12,13,17,54] In parallel, BTK inhibition can reshape immune states, including T-cell subsets and inhibitory receptor programs,[24,25,55-58] raising the possibility that treatment failure reflects coordinated tumor–immune adaptation rather than tumor-intrinsic escape alone. Despite these insights, how tumor subclonal evolution and longitudinal T-cell dynamics jointly shape response to ibrutinib remains poorly understood, and biomarkers that predict response or relapse early are lacking.

To address these challenges, we performed longitudinal single-cell multi-omics profiling within a prospective phase II trial of ibrutinib monotherapy. Across 74 sequential BM samples from 17 WM patients, we analyzed more than 630,000 high-quality cells and reconstructed patient-specific clonal architectures. This revealed three distinct evolutionary patterns: "evolution," "devolution," and "no-evolution," each strongly associated with clinical response. The "evolution" pattern could be detected 6–24 months before progression, suggesting that longitudinal genomic monitoring may serve as an early-warning system for relapse. Similar genomic surveillance approaches have shown promise in CLL and other B-cell malignancies, supporting the feasibility of this strategy in WM.[59-61] Early clonal evolution events were closely associated with subsequent progression, underscoring the potential of genomic monitoring for preemptive intervention.[54]

Within this evolutionary framework, we further showed that baseline tumor architecture constrains subsequent adaptive patterns. The WIP score captured transcriptional features of tumor cells that predisposed to evolutionary escape under ibrutinib. Functionally, we identified *LYN* as a key mediator of resistance captured by the WIP program and demonstrated that dual BTK/LYN inhibition restored sensitivity in resistant models. Consistently, preclinical models have shown that concurrent inhibition of BTK and LYN synergistically induces tumor apoptosis and suppresses compensatory signaling.[8,36,62]

Beyond tumor-intrinsic adaptation, immune remodeling emerged as an integral component of treatment failure. In "evolution" patients, GZMB$^+$ CD8$^+$ TEM cells expanded during therapy but adopted a de-differentiated $CD27^+$ $TCF1^+$ memory-like state with reduced cytotoxicity, increased *PDCD1* expression, and activation of *BCL2* and hypoxia-related programs. This phenotype parallels exhaustion-associated de-differentiation arrest described in chronic infection and tumor settings, where persistent antigen stimulation and metabolic stress drive T cells toward progenitor-like or hyporesponsive states instead of achieving full cytolytic activation.[63-66] Notably, both baseline and post-treatment features of $GZMB^+$ $CD8^+$ TEM cells were tightly correlated with clinical outcomes, underscoring immune dysfunction as a contributor to incomplete tumor clearance.[37,67]

Strikingly, we observed convergent activation of hypoxia-associated pathways in both resistant tumor clones and dysfunctional TEM cells. These findings suggested that metabolic adaptation represents a shared axis of resistance across tumor and immune compartments. Therapeutic strategies targeting hypoxia signaling may attenuate resistance in both tumor and T-cell compartments.[68,69]

Together, our results supported a unified model in which ibrutinib response in WM reflected the outcome of tumor–immune co-evolution under selective pressure. Baseline tumor states shaped evolutionary potential, ibrutinib imposed selective bottlenecks that favored adaptive subclones, and immune dysfunction limited durable tumor control. By integrating the WIP score, longitudinal genomic surveillance, and immune-informed therapeutic targeting, our study outlined a precision framework for managing WM under BTK inhibition that may extend to other B-cell malignancies. Limitations included the modest cohort size and the exploratory nature of the study. The mechanisms driving T-cell reprogramming and strategies to restore durable cytotoxic function warranted further investigation.

In conclusion, our study provides the largest single-cell multi-omics atlas in WM to date, delineating the co-evolution of tumor subclones and T-cell compartments under BTK inhibitor pressure. By defining distinct evolutionary trajectories, establishing a baseline predictor of resistance, identifying actionable signaling dependencies, and uncovering immune dysfunction as a determinant of relapse, our work advances a mechanistic and translational framework for overcoming BTK inhibitor resistance in WM and related B-cell malignancies.

Acknowledgements

This work was supported by the International Waldenström's Macroglobulinemia Foundation Robert A. Kyle Career Development Award (HS) and the Legacy Grant for Dr. Steven Treon; the Leukemia and Lymphoma Society (Blood Cancer United) Translational Research Grant (No. 6673-24); the Peter and Helen Bing Fund for WM Research; the Orszag and Kitchen WM Research Fund; the Paul and Ronnie Siegel Fund for WM Research at DFCI; the Estate of David and Barbara Levine; and the Dordick Law College. Dr. Hunter is supported by the Bliss Family Investigatorship in WM. The authors gratefully acknowledge the patients who provided samples that made this study possible. Samples were derived from a clinical trial supported by Pharmacyclics, which also provided funding for biomarker analysis.

Authorship contributions:

SPT conceived and designed the study. SPT, RSP, and SRL supervised the study and provided conceptual guidance. HS performed the research and conducted the bioinformatic analyses. SRL and SQL performed single-cell multi-omic library preparation and sequencing. HS, XL, SRL, NT, MLG, AK, ALP, and DP processed samples and carried out laboratory experiments. JMH conducted drug synthesis and enzymatic inhibition assays. HS analyzed and interpreted the experimental data. NT, ARG, AG, CAF, CJP, KM, ARB, SRS, JJC, and SPT identified and collected clinical samples and/or analyzed clinical data. SQL, DBK, VC, NK, HL, WL, KJL, and KM provided valuable insights into sample sequencing. RSP, ARB, CJW, IMG, LGQ, SHY, WPY, MH, SRL, ZRH, and SPT provided scientific insights and guidance on data analysis and interpretation. HS and RSP drafted the initial manuscript, and all authors critically revised the paper for important intellectual content.

Conflict-of-interest disclosure: SPT received research funding, and/or consulting fees from Abbvie/Pharmacyclics Inc., Janssen Oncology Inc., Beigene Inc., Eli Lilly Pharmaceuticals, Bristol Myers Squibb, and Ono Pharmaceuticals. JJC received research funds or consulting fees from Abbvie, AstraZeneca, Avilar, BeOne, Cellectar, Johnson & Johnson, LOXO, and Pharmacyclics. SRS received research funding and/or consulting fees from ADC Therapeutics, Beigene, Cellectar, and SOBI. DBK serves as a scientific advisor for Immunitrack (a wholly owned subsidiary of Eli Lilly and Company) and Breakbio, and holds equity in Affimed N.V., Agenus, Armata Pharmaceuticals, Breakbio, BioMarin Pharmaceutical, Celldex Therapeutics, Editas Medicine, ImmunityBio, Lexicon Pharmaceuticals, Moderna, Sana Biotechnology, and Summit Therapeutics. JMH received consulting fees from Arbella Therapeutics. RSP is a co-founder, equity holder and consultant in PreDICTA Biosciences. The remaining authors declare no competing financial interests.

References

1. Owen RG, Treon SP, Al-Katib A, et al. Clinicopathological definition of Waldenstrom's macroglobulinemia: consensus panel recommendations from the Second International Workshop on Waldenstrom's Macroglobulinemia. *Semin Oncol*. 2003;30(2):110-115.
2. Treon SP, Xu L, Yang G, et al. MYD88 L265P somatic mutation in Waldenström's macroglobulinemia. *N Engl J Med*. 2012;367(9):826-833.
3. Yang G, Zhou Y, Liu X, et al. A mutation in MYD88 (L265P) supports the survival of lymphoplasmacytic cells by activation of Bruton tyrosine kinase in Waldenström macroglobulinemia. *Blood*. 2013;122(7):1222-1232.
4. Treon SP, Tripsas CK, Meid K, et al. Ibrutinib in previously treated Waldenström's macroglobulinemia. *N Engl J Med*. 2015;372(15):1430-1440.
5. Dimopoulos MA, Trotman J, Tedeschi A, et al. Ibrutinib for patients with rituximab-refractory Waldenström's macroglobulinaemia (iNNOVATE): an open-label substudy of an international, multicentre, phase 3 trial. *Lancet Oncol*. 2017;18(2):241-250.
6. Treon SP, Meid K, Gustine J, et al. Long-Term Follow-Up of Ibrutinib Monotherapy in Symptomatic, Previously Treated Patients With Waldenström Macroglobulinemia. *J Clin Oncol*. 2021;39(6):565-575.
7. Buske C, Jurczak W, Salem JE, Dimopoulos MA. Managing Waldenström's macroglobulinemia with BTK inhibitors. *Leukemia*. 2023;37(1):35-46.
8. Liu TM, Woyach JA, Zhong Y, et al. Hypermorphic mutation of phospholipase C, γ2 acquired in ibrutinib-resistant CLL confers BTK independency upon B-cell receptor

activation. *Blood*. 2015;126(1):61-68.

9. Woyach JA, Furman RR, Liu TM, et al. Resistance mechanisms for the Bruton's tyrosine kinase inhibitor ibrutinib. *N Engl J Med*. 2014;370(24):2286-2294.

10. Chen JG, Liu X, Munshi M, et al. BTK(Cys481Ser) drives ibrutinib resistance via ERK1/2 and protects BTK(wild-type) MYD88-mutated cells by a paracrine mechanism. *Blood*. 2018;131(18):2047-2059.

11. Tam CS, Opat S, D'Sa S, et al. Biomarker analysis of the ASPEN study comparing zanubrutinib with ibrutinib for patients with Waldenström macroglobulinemia. *Blood Adv*. 2024;8(7):1639-1650.

12. Amin NA, Balasubramanian S, Saiya-Cork K, Shedden K, Hu N, Malek SN. Cell-Intrinsic Determinants of Ibrutinib-Induced Apoptosis in Chronic Lymphocytic Leukemia. *Clin Cancer Res*. 2017;23(4):1049-1059.

13. Kanagal-Shamanna R, Jain P, Patel KP, et al. Targeted multigene deep sequencing of Bruton tyrosine kinase inhibitor-resistant chronic lymphocytic leukemia with disease progression and Richter transformation. *Cancer*. 2019;125(4):559-574.

14. Cao Y, Hunter ZR, Liu X, et al. The WHIM-like CXCR4(S338X) somatic mutation activates AKT and ERK, and promotes resistance to ibrutinib and other agents used in the treatment of Waldenstrom's Macroglobulinemia. *Leukemia*. 2015;29(1):169-176.

15. Cao Y, Hunter ZR, Liu X, et al. CXCR4 WHIM-like frameshift and nonsense mutations promote ibrutinib resistance but do not supplant MYD88(L265P) -directed survival signalling in Waldenström macroglobulinaemia cells. *Br J Haematol*. 2015;168(5):701-707.

16. Gustine JN, Xu L, Tsakmaklis N, et al. CXCR4(S338X) clonality is an important determinant of ibrutinib outcomes in patients with Waldenström macroglobulinemia. *Blood Adv*. 2019;3(19):2800-2803.

17. Jiménez C, Chan GG, Xu L, et al. Genomic evolution of ibrutinib-resistant clones in Waldenström macroglobulinaemia. *Br J Haematol*. 2020;189(6):1165-1170.

18. Gustine JN, Sarosiek S, Flynn CA, et al. Natural history of Waldenström macroglobulinemia following acquired resistance to ibrutinib monotherapy. *Haematologica*. 2022;107(5):1163-1171.

19. Richardson K, Castillo JJ, Sarosiek SR, et al. Identification of robust predictors for ibrutinib response by multiomics in MYD88-mutated Waldenström macroglobulinemia. *Blood Adv*. 2024;8(9):2133-2137.

20. Greaves M, Maley CC. Clonal evolution in cancer. *Nature*. 2012;481(7381):306-313.

21. McGranahan N, Swanton C. Clonal Heterogeneity and Tumor Evolution: Past, Present, and the Future. *Cell*. 2017;168(4):613-628.

22. Sun H, Fang T, Wang T, et al. Single-cell profiles reveal tumor cell heterogeneity and immunosuppressive microenvironment in Waldenström macroglobulinemia. *J Transl Med*. 2022;20(1):576.

23. Gagler DC, Ghamlouch H, Zhang D, et al. A multiomic analysis of Waldenström macroglobulinemia defines distinct disease subtypes. *Blood*. 2025;146(10):1225-1238.

24. Long M, Beckwith K, Do P, et al. Ibrutinib treatment improves T cell number and function in CLL patients. *J Clin Invest*. 2017;127(8):3052-3064.

25. Liu Y, Song Y, Yin Q. Effects of ibrutinib on T-cell immunity in patients with chronic lymphocytic leukemia. *Front Immunol*. 2022;13:962552.

26. Castillo JJ, Meid K, Gustine JN, et al. Long-term follow-up of ibrutinib monotherapy in treatment-naive patients with Waldenstrom macroglobulinemia. *Leukemia*. 2022;36(2):532-539.

27. Zheng GX, Terry JM, Belgrader P, et al. Massively parallel digital transcriptional profiling of single cells. *Nat Commun*. 2017;8:14049.

28. Wolf FA, Angerer P, Theis FJ. SCANPY: large-scale single-cell gene expression data analysis. *Genome Biol*. 2018;19(1):15.

29. Sturm G, Szabo T, Fotakis G, et al. Scirpy: a Scanpy extension for analyzing single-cell T-cell receptor-sequencing data. *Bioinformatics*. 2020;36(18):4817-4818.

30. Gao T, Soldatov R, Sarkar H, et al. Haplotype-aware analysis of somatic copy number variations from single-cell transcriptomes. *Nat Biotechnol*. 2023;41(3):417-426.

31. Muzellec B, Teleńczuk M, Cabeli V, Andreux M. PyDESeq2: a python package for bulk RNA-seq differential expression analysis. *Bioinformatics*. 2023;39(9).

32. Krämer A, Green J, Pollard J, Jr., Tugendreich S. Causal analysis approaches in Ingenuity Pathway Analysis. *Bioinformatics*. 2014;30(4):523-530.

33. Fang Z, Liu X, Peltz G. GSEApy: a comprehensive package for performing gene set enrichment analysis in Python. *Bioinformatics*. 2023;39(1).

34. Büttner M, Ostner J, Müller CL, Theis FJ, Schubert B. scCODA is a Bayesian model for compositional single-cell data analysis. *Nat Commun*. 2021;12(1):6876.

35. Owen RG, Kyle RA, Stone MJ, et al. Response assessment in Waldenström

macroglobulinaemia: update from the VIth International Workshop. *Br J Haematol*. 2013;160(2):171-176.

36. Song Y, Zhou K, Jing H, et al. Phase 1/2 Studies of DZD8586, a Non-Covalent BBB Penetrant LYN/BTK Dual Inhibitor, in BTK Inhibitor Resistant Chronic Lymphocytic Leukemia (CLL) and Other B-Cell Non-Hodgkin Lymphoma (B-NHL). *Blood*. 2024;144:3248.

37. Sklavenitis-Pistofidis R, Aranha MP, Redd RA, et al. Immune biomarkers of response to immunotherapy in patients with high-risk smoldering myeloma. *Cancer Cell*. 2022;40(11):1358-1373.e1358.

38. Buske C, Tedeschi A, Trotman J, et al. Ibrutinib Plus Rituximab Versus Placebo Plus Rituximab for Waldenström's Macroglobulinemia: Final Analysis From the Randomized Phase III iNNOVATE Study. *J Clin Oncol*. 2022;40(1):52-62.

39. O'Brien S, Furman RR, Coutre S, et al. Single-agent ibrutinib in treatment-naïve and relapsed/refractory chronic lymphocytic leukemia: a 5-year experience. *Blood*. 2018;131(17):1910-1919.

40. Byrd JC, Brown JR, O'Brien S, et al. Ibrutinib versus ofatumumab in previously treated chronic lymphoid leukemia. *N Engl J Med*. 2014;371(3):213-223.

41. Hampel PJ, Ding W, Call TG, et al. Rapid disease progression following discontinuation of ibrutinib in patients with chronic lymphocytic leukemia treated in routine clinical practice. *Leuk Lymphoma*. 2019;60(11):2712-2719.

42. Epperla N, Hamadani M, Cashen AF, et al. Predictive factors and outcomes for ibrutinib therapy in relapsed/refractory mantle cell lymphoma-a "real world" study.

Hematol Oncol. 2017;35(4):528-535.

43. Martin P. Ibrutinib--a new standard treatment for relapsed mantle cell lymphoma? *Lancet*. 2016;387(10020):728-729.

44. Cervantes-Gomez F, Kumar Patel V, Bose P, Keating MJ, Gandhi V. Decrease in total protein level of Bruton's tyrosine kinase during ibrutinib therapy in chronic lymphocytic leukemia lymphocytes. *Leukemia*. 2016;30(8):1803-1804.

45. Quinquenel A, Fornecker LM, Letestu R, et al. Prevalence of BTK and PLCG2 mutations in a real-life CLL cohort still on ibrutinib after 3 years: a FILO group study. *Blood*. 2019;134(7):641-644.

46. Ahn IE, Underbayev C, Albitar A, et al. Clonal evolution leading to ibrutinib resistance in chronic lymphocytic leukemia. *Blood*. 2017;129(11):1469-1479.

47. Kuo HP, Ezell SA, Schweighofer KJ, et al. Combination of Ibrutinib and ABT-199 in Diffuse Large B-Cell Lymphoma and Follicular Lymphoma. *Mol Cancer Ther*. 2017;16(7):1246-1256.

48. Cosson A, Chapiro E, Bougacha N, et al. Gain in the short arm of chromosome 2 (2p+) induces gene overexpression and drug resistance in chronic lymphocytic leukemia: analysis of the central role of XPO1. *Leukemia*. 2017;31(7):1625-1629.

49. Agarwal R, Chan YC, Tam CS, et al. Dynamic molecular monitoring reveals that SWI-SNF mutations mediate resistance to ibrutinib plus venetoclax in mantle cell lymphoma. *Nat Med*. 2019;25(1):119-129.

50. Rahal R, Frick M, Romero R, et al. Pharmacological and genomic profiling identifies NF-κB-targeted treatment strategies for mantle cell lymphoma. *Nat Med*.

2014;20(1):87-92.

51. Wu C, de Miranda NF, Chen L, et al. Genetic heterogeneity in primary and relapsed mantle cell lymphomas: Impact of recurrent CARD11 mutations. *Oncotarget*. 2016;7(25):38180-38190.

52. Xu L, Tsakmaklis N, Yang G, et al. Acquired mutations associated with ibrutinib resistance in Waldenström macroglobulinemia. *Blood*. 2017;129(18):2519-2525.

53. Li J, Huang Y, Zhang Y, et al. Identification BCL6 and miR-30 family associating with Ibrutinib resistance in activated B-cell-like diffuse large B-cell lymphoma. *Med Oncol*. 2021;38(4):33.

54. Landau DA, Sun C, Rosebrock D, et al. The evolutionary landscape of chronic lymphocytic leukemia treated with ibrutinib targeted therapy. *Nat Commun*. 2017;8(1):2185.

55. Niemann CU, Herman SE, Maric I, et al. Disruption of in vivo Chronic Lymphocytic Leukemia Tumor-Microenvironment Interactions by Ibrutinib--Findings from an Investigator-Initiated Phase II Study. *Clin Cancer Res*. 2016;22(7):1572-1582.

56. Cadot S, Audebert C, Dion C, et al. New pharmacodynamic parameters linked with ibrutinib responses in chronic lymphocytic leukemia: Prospective study in real-world patients and mathematical modeling. *PLoS Med*. 2024;21(7):e1004430.

57. Kondo K, Shaim H, Thompson PA, et al. Ibrutinib modulates the immunosuppressive CLL microenvironment through STAT3-mediated suppression of regulatory B-cell function and inhibition of the PD-1/PD-L1 pathway. *Leukemia*. 2018;32(4):960-970.

58. Rendeiro AF, Krausgruber T, Fortelny N, et al. Chromatin mapping and single-cell

immune profiling define the temporal dynamics of ibrutinib response in CLL. *Nat Commun*. 2020;11(1):577.

59. Fürstenau M, Giza A, Weiss J, et al. Acalabrutinib, venetoclax, and obinutuzumab in relapsed/refractory CLL: final efficacy and ctDNA analysis of the CLL2-BAAG trial. *Blood*. 2024;144(3):272-282.

60. Yeh P, Hunter T, Sinha D, et al. Circulating tumour DNA reflects treatment response and clonal evolution in chronic lymphocytic leukaemia. *Nat Commun*. 2017;8:14756.

61. Fu L, Zhou X, Zhang X, et al. Circulating tumor DNA in lymphoma: technologies and applications. *J Hematol Oncol*. 2025;18(1):29.

62. Bai Y, Wu T, Hu M, et al. Preclinical Study of DZD8586, a Non-Covalent LYN/BTK Dual Inhibitor with Excellent BBB Penetration, for the Treatment of B-Cell Non-Hodgkin Lymphoma (B-NHL). *Blood*. 2023;142:2822.

63. Siddiqui I, Schaeuble K, Chennupati V, et al. Intratumoral Tcf1(+)PD-1(+)CD8(+) T Cells with Stem-like Properties Promote Tumor Control in Response to Vaccination and Checkpoint Blockade Immunotherapy. *Immunity*. 2019;50(1):195-211.e110.

64. Beltra JC, Manne S, Abdel-Hakeem MS, et al. Developmental Relationships of Four Exhausted CD8(+) T Cell Subsets Reveals Underlying Transcriptional and Epigenetic Landscape Control Mechanisms. *Immunity*. 2020;52(5):825-841.e828.

65. Chen Z, Ji Z, Ngiow SF, et al. TCF-1-Centered Transcriptional Network Drives an Effector versus Exhausted CD8 T Cell-Fate Decision. *Immunity*. 2019;51(5):840-855.e845.

66. Pais Ferreira D, Silva JG, Wyss T, et al. Central memory CD8(+) T cells derive from

stem-like Tcf7(hi) effector cells in the absence of cytotoxic differentiation. *Immunity*. 2020;53(5):985-1000.e1011.

67. Botta C, Perez C, Larrayoz M, et al. Large T cell clones expressing immune checkpoints increase during multiple myeloma evolution and predict treatment resistance. *Nature Communications*. 2023;14(1):5825.

68. Alicea Pauneto CDM, Riesenberg BP, Gandy EJ, et al. Intra-tumoral hypoxia promotes CD8(+) T cell dysfunction via chronic activation of integrated stress response transcription factor ATF4. *Immunity*. 2025.

69. Muz B, de la Puente P, Azab F, Azab AK. The role of hypoxia in cancer progression, angiogenesis, metastasis, and resistance to therapy. *Hypoxia (Auckl)*. 2015;3:83-92.

Figure legends

Fig. 1 | Longitudinal single-cell multi-omics profiling of bone marrow (BM) cells from WM patients treated with ibrutinib.

(A) Schematic overview of sample collection and treatment response in the ibrutinib monotherapy clinical trial. The y-axis lists individual patient identifiers, and the x-axis indicates follow-up time points (baseline; cycle 6 [C6, 6 months, 6mo], cycle 12 [C12, 1 year, 1y], cycle 24 [C24, 2 years, 2y], cycle 36 [C36, 3 years, 3y], and cycle 48 [C48, 4 years, 4y]). Colored circles denote clinical response categories: very good partial response (VGPR), partial response (PR), minor response (MR), stable disease (SD), progressive disease (PD), and not available (NA). Black triangles mark time points at which BM aspirates were collected for single-cell multi-omic profiling (scRNA-seq, BCR, and TCR sequencing).

(B) UMAP visualization of all BM cells passing quality control (n = 634,414), with each dot representing a single cell. Colors indicate groupings or V(D)J/*CD19*/C*D3E* expression. Five panels illustrate patient origin, treatment time point, response category, TCR and BCR abundance, and cell type along with *CD19* and *CD3E* expression (natural log-transformed, normalized UMI counts). B/plasma cell and T-cell clusters are labeled. TCR abundance denotes the number of T cells sharing the same TCR. BCR abundance denotes the number of B/plasma cells sharing the same BCR.

(C) UMAP visualization of reclustered B/plasma cells (n = 148,458), with dots colored by subgroup. The five panels display patient origin, treatment time point, response category, BCR clonotype, and cell subtype. Normal B/plasma cell populations are annotated.

(D) UMAP visualization of reclustered T cells (n = 286,077), with dots colored by subgroup. The four panels show patient origin, treatment time point, response category, TCR abundance, and cell subtype.

Fig. 2 | Tumor clonal phylogenies and evolutionary patterns associated with response to ibrutinib in WM patients.

(A) UMAP visualization of reclustered B/plasma cells from a representative patient with disease progression (W010). Each dot represents a single cell, colored by subgroup identity or pseudotime order. Six panels display cell subtypes, BCR clonotypes, CNV-based tumor clones, transcriptome-defined subclusters, pseudotime trajectories, and treatment cycle. Black line segments denote pseudotime differentiation paths inferred from transcriptomic data. The last three panels pertain to primary tumor 1.

(B) Left: clonal phylogenetic tree of W010 reconstructed from CNV-based tumor clones (each vertical color denotes a clone; x-axis indicates number of CNVs; connecting lines indicate evolutionary order). Right: copy-number profiles of each clone (red = amplification; blue = deletion; grey = neutral).

(C) Top: line plot showing longitudinal serum IgM levels (solid dots/lines; colors indicate treatment response) and tumor burden (hollow dots, dashed lines; assessed as percentage of intertrabecular lymphoplasmacytic cells from BM biopsy) across treatment cycles in W010. Bottom: fishplot depicting relative proportions of the three tumor clones at baseline and post-treatment cycles. Changes relative to baseline were calculated using scCODA Bayesian modeling of compositional data; asterisks indicate statistical significance (FDR < 0.05).

(D) UMAP visualization of reclustered B/plasma cells from a representative patient with sustained remission (W003). Each dot represents a single cell, colored by subgroup identity or pseudotime order. Six panels display cell subtypes, BCR clonotypes, CNV-based tumor clones, transcriptome-defined subclusters, pseudotime trajectories, and treatment cycle. Black line segments denote transcriptome-inferred pseudotime paths.

(E) Left: CNV-based clonal phylogenetic tree of W003 (vertical colors represent clones; x-axis indicates number of CNVs; connecting lines indicate evolutionary order). Right: copy-number profiles of each clone (red = amplification; blue = deletion; grey = neutral).

(F) Top: line plot showing longitudinal serum IgM levels (solid dots/lines; colors indicate treatment response) and tumor burden (hollow dots, dashed lines; proportion of intertrabecular lymphoplasmacytic cells) in W003. Bottom: fishplot depicting relative proportions of three tumor clones at baseline and post-treatment cycles, with statistical testing by scCODA (FDR < 0.05).

(G) Stacked bar plot showing the proportions of tumor clone (for patients with detectable CNVs) or transcriptome-defined tumor clusters (for patients lacking CNVs) across baseline and post-treatment cycles. Each column represents one sample. Post-treatment changes relative to baseline were assessed using scCODA (FDR < 0.05, asterisks). Annotation tracks below indicate, from top to bottom: patient ID, treatment cycle, post-treatment response at each time point, responder vs non-responder status, and clonal evolutionary pattern.

Fig. 3 | Transcriptomic scoring based on resistant clones predicts ibrutinib efficacy, with *LYN* identified as a core resistance gene and functional validation of BTK/LYN dual inhibition in overcoming resistance.

(A) Protein–protein interaction (PPI) network generated by STRING showing 130 shared differentially expressed genes (DEGs) from resistant clones in patients with disease progression, organized into 10 functional gene clusters. Different colors denote distinct gene clusters, and each node represents a gene. The size of each circle indicates connectivity with other members of the network, while the border color reflects expression direction (red, upregulated; blue, downregulated). Colored edges represent interactions with genes within the same cluster, whereas grey edges represent inter-cluster interactions. Upward and downward arrows indicate overall up- or down-regulation of each gene cluster, calculated using Ingenuity Pathway Analysis (IPA) z-scores.

(B) Bar plot depicting the representative functional pathways of the 10 gene clusters identified by STRING. The y-axis represents gene clusters, and the x-axis represents the $-\log_{10}(\mathrm{FDR})$ enrichment values derived from over-representation analysis.

(C) Bar plot showing the mean gene importance of genes within the Waldenström's Ibrutinib Prediction (WIP) score gene set. The x-axis denotes 30 genes with mean gene importance > 0.6, and the y-axis indicates gene importance. Gene importance was calculated as the sum of the min–max normalized absolute $\log_2$ fold change in resistant clones and the min–max normalized connectivity of the gene in the PPI network. Connectivity and gene importance were estimated by randomly sampling 100 genes from the PPI network 100 times. Error bars represent SEM of mean gene importance. Bar border colors indicate direction of expression (red, upregulated; blue, downregulated). Statistical significance of gene importance differences was tested by Kruskal–Wallis test.

(D) Kaplan–Meier curves comparing progression incidence under ibrutinib treatment between patients with high vs. low WIP scores. Hazard ratios (HRs) and 95% confidence intervals (CIs) were calculated by Cox proportional hazards regression, and *P* values were derived from log-rank tests. Risk tables display the number of patients at risk at each time point.

(E) Western blot showing the effects of *LYN* knockdown on total and phosphorylated proteins in multiple signaling pathways in BCWM.1 and MWCL-1 cells. Two independent shRNAs (*LYN*-KD #1 and *LYN*-KD #2) were used for knockdown. Scr denotes scramble controls. GAPDH served as a protein loading control. we performed densitometric analysis using ImageJ (version 1.54p) to obtain semi-quantitative measurements of phosphorylated protein levels. For each protein band, the mean gray value was extracted and normalized to the corresponding GAPDH band within the same sample to account for loading variability. Phospho-protein levels were quantified by densitometric analysis using ImageJ, normalized to GAPDH, and expressed relative to the scramble control.

(F) Dose–response curves of cell viability in *LYN*-knockdown vs. scramble MWCL-1 cells after 72 hours of treatment with increasing concentrations of ibrutinib, measured by CellTiter-Glo assay. The y-axis indicates viability normalized to DMSO controls, and the x-axis denotes drug concentration ($\log_{10}$-transformed). Statistical analysis was performed using two-way ANOVA.

(G) Schematic diagram of the stepwise induction of ibrutinib-resistant cell lines. Naïve BCWM.1 and MWCL-1 cells were progressively exposed to increasing concentrations of ibrutinib (0.05 µM to 3.0 µM), with 2–3 passages per dose and cell medium refreshed every 2 days, over ~5 months.

(H) Dose–response curves showing cell viability of naïve (BCWM.1, MWCL-1) and resistant (BCWM.1R, MWCL-1R) WM cells treated with ibrutinib alone for 72 hours, measured by CellTiter-Glo assay. The y-axis represents viability normalized to DMSO controls, and the x-axis denotes drug concentration ($\log_{10}$-transformed). Statistical testing was performed using two-way ANOVA.

(I) Bar plot comparing *LYN* mRNA expression in naïve vs. ibrutinib-resistant BCWM.1 and MWCL-1 cells. TaqMan qPCR assays were normalized to *GAPDH* (ΔCt), and relative expression was calculated by the 2^(-ΔΔCt) method, with naïve cells serving as calibrators (mean = 1). Bars represent mean ± SEM. Statistical comparisons were performed using two-sided Wilcoxon rank-sum test.

(J) Dose–response curves showing cell viability of naïve and ibrutinib-resistant MWCL-1 (MWCL-1, MWCL-1R) cells treated with ibrutinib alone, a BTK/LYN dual inhibitor (BTKi/LYNi), or DMSO control for 72 hours, measured by CellTiter-Glo assay. The y-axis represents viability normalized to DMSO controls, and the x-axis denotes drug concentration ($\log_{10}$-transformed). Statistical testing was performed using two-way ANOVA.

(K) Western blot of total and phosphorylated BTK and LYN proteins in naïve and resistant BCWM.1 and MWCL-1 cells treated for 16 hours with 0.5 µM ibrutinib or 0.5 µM BTKi/LYNi. GAPDH served as a protein loading control. Phospho-protein levels were quantified by densitometric analysis using ImageJ, normalized to GAPDH, and expressed relative to the scramble control.

Fig. 4 | Divergent pathway activities between early and late tumor clones in "evolution" patients under ibrutinib treatment, with in vitro validation of post-treatment hypoxia

signaling.

(A) Bubble plot showing pathway activity differences between early (left) and late (right) tumor clones from “evolution” patients (W013, W010, W011, and W012) at multiple treatment cycles (C6–C48), each compared to the baseline stage. The y-axis displays the 27 pathways significantly affected by ibrutinib, and the x-axis indicates sampling timepoints from different patients. Bubble color represents the direction and magnitude of enrichment (IPA-derived z-score; red, upregulated; blue, downregulated), while bubble size reflects significance ($-\log_{10}$ *P*-value). Circles with black borders denote significant differences ($P < 0.05$). Annotation tracks at the bottom indicate treatment cycle, patient ID, and post-treatment response status. Green boxes highlight pathways with significant changes observed in at least 75% of patients at the timepoint.

(B) Violin plots depicting the dynamic changes in hypoxia signaling between early and late tumor clones in “evolution” patients at baseline and subsequent post-treatment cycles. Hypoxia scores were calculated using GSVA method and normalized by min–max scaling within each patient. The y-axis shows GSVA scores, and the x-axis represents treatment cycles. Colored dots within violins indicate group medians. LOESS curves fitted with geom_smooth are shown (red, late clones; teal, early clones) with shaded 95% confidence intervals. Statistical significance was assessed by two-way ANOVA.

(C) Violin plots with overlaid boxplots illustrating *HIF1A* expression in late tumor clones from patients W010, W013, and W011 at baseline and across post-treatment cycles (C6–C48). White dots within violins indicate medians. The red curve represents LOESS fitting (using the statsmodels package), with shaded areas denoting 95% confidence intervals. Statistical testing was performed with the Kruskal–Wallis test.

(D) Immunofluorescence staining of naïve and ibrutinib-resistant BCWM.1 (BCWM.1, BCWM.1R) cells after treatment with DMSO or 1 μM ibrutinib for 24 h, showing HIF-1α expression. Staining included HIF-1α (purple), CD19 (green), DAPI (blue), and merged images. Scale bar, 20 μm.

(E) Flow cytometry analysis of HIF-1α expression in naïve and ibrutinib-resistant cells treated with DMSO or 1 μM ibrutinib for 24 h. Left, normalized density plots (HIF-1α–PE channel) for BCWM.1/BCWM.1R (top) and MWCL-1/MWCL-1R (bottom) cells, with isotype control as negative reference. Right, corresponding boxplots summarizing HIF-1α expression across groups. Statistical comparisons were performed using the two-sided Wilcoxon rank-sum test.

Fig. 5 | Large expansion of GZMB$^+$ CD8$^+$ TEM cells with reduced cytotoxicity and de-differentiation into CD27$^+$ TCF7$^+$ memory T cells in “evolution” patients under ibrutinib treatment.

(A) UMAP plots of all T cells showing T-cell subtype (left) and clone grouping (right). Each dot represents a single cell. In the right panel, clone groups are defined as: Large clone (red; >10% of all T cells in each sample), Medium clone (yellow; 1–10%), and Small clone (blue; <1%).

(B) Line plots showing dynamic changes in TCR diversity (measured by the Chao1 index) across baseline and post-treatment cycles (C6–C48) in patients stratified by three clonal evolutionary patterns of tumor cells. To account for differences in cell numbers across sample, 100 T cells were randomly sampled without replacement 100 times per sample, and the mean Chao1 index was calculated. Colored dots and connecting lines represent the mean

TCR diversity of individual patients across post-treatment cycles. The three smooth curves with shaded areas indicate the overall fitted trends and 95% confidence intervals for the three clonal evolutionary groups: green for “devolution”, gray for “no-evolution”, and purple for “evolution”. Curves were fitted using the geom_smooth function with the LOESS method. Statistical comparisons were performed using two-way ANOVA.

(C) Stacked bar plots showing the proportions of T cell clone groups across patients at baseline and different post-treatment cycles (C6–C48). Colors denote clone groups, and each column represents one sample. Annotation tracks below indicate patient ID, treatment cycle, treatment response at each timepoint, overall responder status, and clonal evolutionary pattern. Colors correspond to different categories.

(D) Concentric ring plots showing the hierarchical relationship between T-cell clones and T-cell clusters in “evolution” patients (W013, W010, W011, and W012). The entire circle represents all T cells (100%) from each patient, with the area of each inner sector corresponding to the proportion of cells. The innermost ring denotes individual T-cell clones (each color representing one clone; only the top 10 clones per patient are shown, with the remainder grouped as “others”), the middle ring represents clone groups (Small, Medium, Large), and the outer ring indicates the corresponding functional T-cell clusters.

(E) Line plots showing dynamic changes in the proportion of GZMB$^+$ CD8$^+$ TEM (KIR$^-$) cells among total T cells at baseline and post-treatment cycles (C6–C48) across different clonal evolutionary groups. Colored dots and lines represent individual patients. Smoothed LOESS curves with 95% confidence intervals are shown for the three groups (green, gray, and purple). Two-way ANOVA was used for statistical testing.

(F) Boxplots of cytotoxicity scores for GZMB$^+$ CD8$^+$ TEM cells (KIR$^+$ or KIR$^-$) in patients exhibiting large T cell expansion. The x-axis indicates treatment stages, and colors denote clone groups. Missing boxes indicate absence of that clone group at the corresponding timepoint. Two-sided Wilcoxon rank-sum test for two groups, Kruskal–Wallis test for 3 groups.

(G) Volcano plot of DEGs between GZMB$^+$ CD8$^+$ TEM cells with large expansion and those without expansion (small clone) in patients W013, W010, and W011. The x-axis represents $\log_2$ fold change, and the y-axis shows significance ($-\log_{10}$ adjusted *P*-value). Differential testing was performed using the two-sided Wilcoxon rank-sum test implemented in scanpy. Genes were considered significant at adjusted $P < 0.05$ and $|\log_2 \text{fold change}| > 0.25$. Dots are colored by differential direction (red, upregulated; blue, downregulated), and dot size reflects significance. Representative DEGs are labeled.

(H) Line plots showing dynamic changes in cytotoxicity scores of GZMB$^+$ CD8$^+$ TEM cells across baseline and post-treatment cycles (C6–C48) in patients grouped by three clonal evolutionary patterns. Colored dots and lines indicate individual patients. Smoothed LOESS curves with 95% confidence intervals are shown for the three groups (green, gray, and purple). Two-way ANOVA was used for statistical testing.

(I) Heatmap showing expression of DEGs identified between “evolution” and “devolution” patients within GZMB$^+$ CD8$^+$ TEM cells across all patient samples. The x-axis denotes genes, and the y-axis represents patient samples. Expression values were scaled per gene (mean = 0, SD = 1 across all samples). Red indicates upregulation, and blue indicates downregulation. Left-side annotation tracks indicate patient ID, treatment cycle, and clonal evolutionary pattern.

Fig. 6 | Baseline transcriptional differences in GZMB$^+$ CD8$^+$ TEM cells between ibrutinib responders and non-responders.

(A) Volcano plot of DEGs in GZMB$^+$ CD8$^+$ TEM cells at baseline between non-responders and responders to ibrutinib treatment. A total of 28 genes were upregulated and 30 genes were downregulated. The x-axis represents $\log_2$ fold change, and the y-axis shows statistical significance ($-\log_{10}$ adjusted *P*-value). Differential expression was assessed using a pseudobulk approach implemented in PyDESeq2. Genes were considered significant at adjusted $P < 0.05$ and $|\log_2 \text{fold change}| > 0.25$. Dots are colored by direction of regulation (red, upregulated; blue, downregulated), with dot size reflecting significance level. Representative DEGs are labeled.

(B) Heatmap showing expression of DEGs in GZMB$^+$ CD8$^+$ TEM cells at baseline between responders and non-responders. The x-axis denotes genes, and the y-axis represents patient samples. Expression values were scaled per gene (mean = 0, SD = 1 across all samples). Red indicates upregulation, and blue indicates downregulation. Left-side annotation tracks indicate treatment response status (Responder: Yes/No), patient ID, and clonal evolutionary pattern.

(C) Left: violin plots with overlaid boxplots showing *GNLY* expression in baseline GZMB$^+$ CD8$^+$ TEM cells from responders and non-responders. Right: violin/boxplots of the non-responding TEM score between the two groups. Individual points are colored by patient. Statistical comparisons were performed with the two-sided Wilcoxon rank-sum test, and the area under the ROC curve (AUC) was calculated. Dashed lines indicate optimal ROC cutoffs.

(D) Scatter plots with regression lines showing correlations at baseline between tumor cell WIP scores and *GNLY* expression in GZMB$^+$ CD8$^+$ TEM cells (left), and between WIP scores and the non-responder TEM score of GZMB$^+$ CD8$^+$ TEM cells (right). Dots are colored by patient. Linear regression was used for fitting; shaded areas represent 95% confidence intervals. Correlations were tested with Pearson's method, and correlation coefficients (*r*) with *P* values are shown.

(E) Heatmap showing expression of the non-responder TEM signature in GZMB$^+$ CD8$^+$ TEM cells from healthy donors (HD) and from baseline WM samples stratified by clinical response (responder vs non-responder). The x-axis denotes signature genes and the y-axis denotes patient samples. Expression values were scaled per gene (mean = 0, SD = 1 across all samples). Left-side annotation tracks indicate sample group (HD vs WM), response status (WM only; responder: yes/no), and individual sample identity.

(F) Violin plots comparing *GNLY* expression (top) and the non-responder TEM score (bottom) in GZMB$^+$ CD8$^+$ TEM cells across HD, responders, and non-responders. Top, GNLY expression; bottom, non-responder TEM score. Each dot represents one patient sample; boxplots indicate the median and interquartile range. Statistical testing was performed using the Kruskal–Wallis test followed by Dunn's multiple comparisons test with Holm adjustment (two-sided).

(G) Violin plots comparing *PDCD1* expression in GZMB$^+$ CD8$^+$ TEM cells between HD and WM samples. Statistical comparisons were performed using the two-sided Wilcoxon rank-sum test.

(H) Violin plots comparing *PDCD1* expression in GZMB$^+$ CD8$^+$ TEM cells from WM patients stratified by clonal evolutionary pattern (Devolution, No-evolution, Evolution). Statistical testing was performed using the Kruskal–Wallis test followed by Dunn's multiple comparisons test with Holm adjustment (two-sided).

(I) Schematic diagram summarizing dynamic tumor clone and T-cell changes in patients with disease progression under ibrutinib treatment (from baseline to post-treatment, left to right). In progressing patients, late tumor clones at baseline exhibit increased *LYN* expression, elevated WIP scores, and complex CNVs. During ibrutinib treatment, early tumor clones gradually diminish while late clones expand, leading to clonal shift, accompanied by increased HIF-1α expression in late clones. In parallel, GZMB$^+$ CD8$^+$ TEM cells from progressing patients exhibited higher baseline *PDCD1* and lower *GNLY* expression, and expanded after treatment with increased hypoxia signaling and upregulation of *BCL2, CD27,* and *TCF7*, while remaining persistently low in cytotoxicity.

Figure 1

Fig. 1

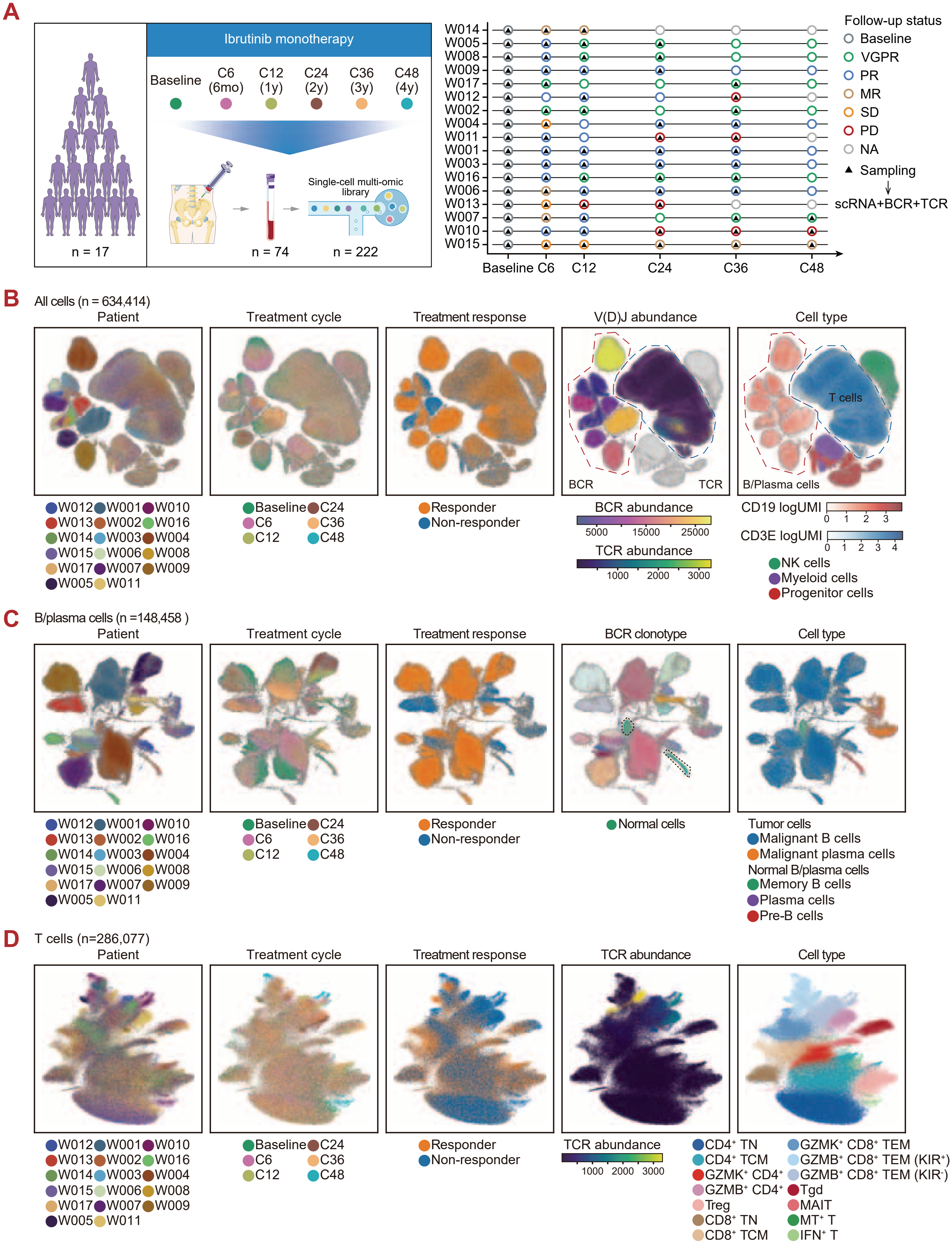

Fig. 2

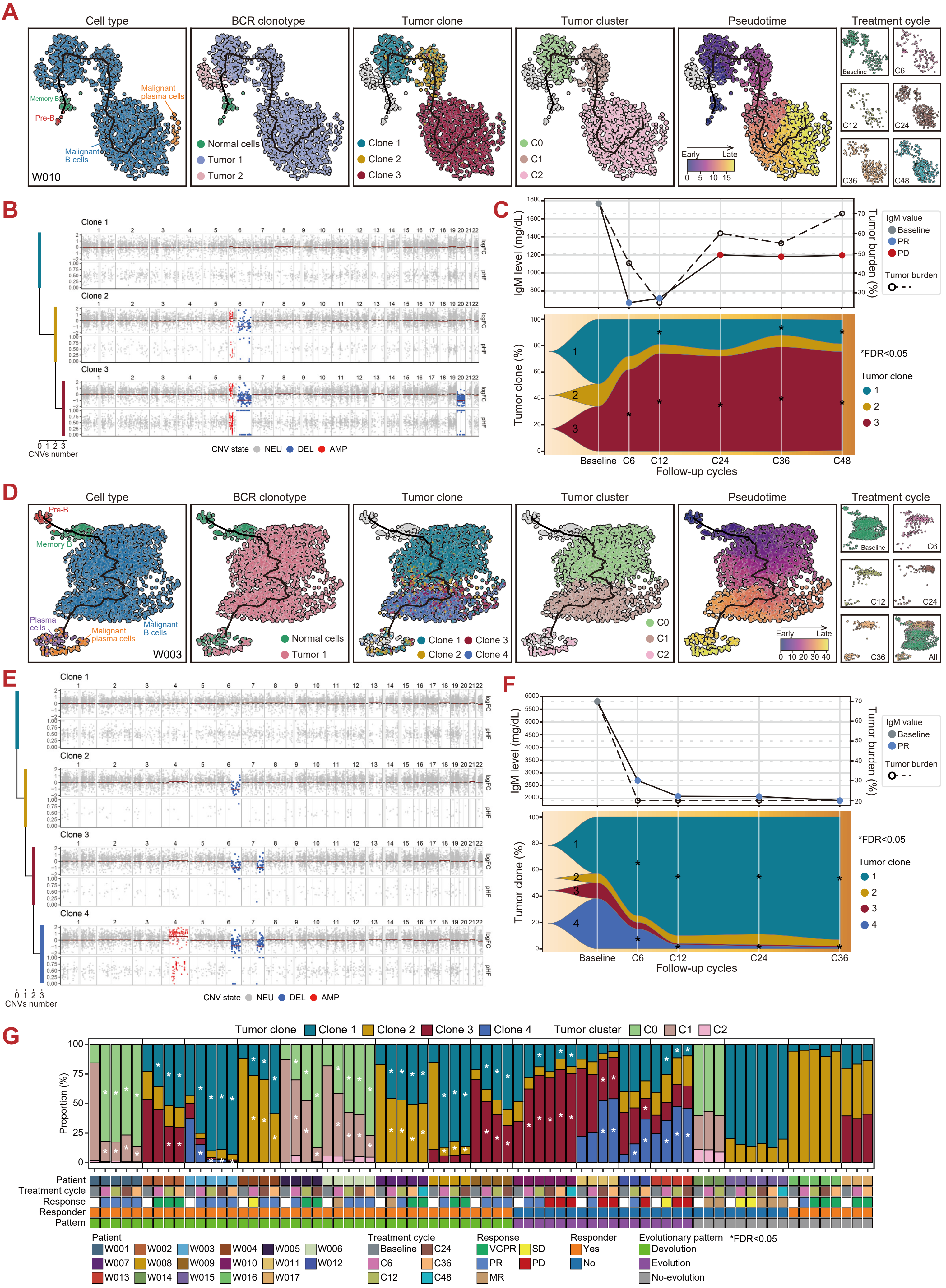
A
Cell type
BCR clonotype
Tumor clone
Tumor cluster
Pseudotime
Treatment cycle
Memory B
Pre-B
Malignant plasma cells
Malignant B cells
W010
Normal cells
Tumor 1
Tumor 2
Clone 1
Clone 2
Clone 3
C0
C1
C2
Early
Late
0 5 10 15
Baseline
C6
C12
C24
C36
C48
B
Clone 1
Clone 2
Clone 3
logFC
pHF
0 1 2 3
CNVs number
CNV state NEU DEL AMP
C
IgM level (mg/dL)
Tumor burden (%)
IgM value
Baseline
PR
PD
Tumor burden
Tumor clone (%)
*FDR<0.05
Tumor clone
1
2
3
Baseline C6 C12 C24 C36 C48
Follow-up cycles
D
Cell type
BCR clonotype
Tumor clone
Tumor cluster
Pseudotime
Treatment cycle
Pre-B
Memory B
Plasma cells
Malignant plasma cells
Malignant B cells
W003
Normal cells
Tumor 1
Clone 1
Clone 2
Clone 3
Clone 4
C0
C1
C2
Early
Late
0 10 20 30 40
Baseline
C6
C12
C24
C36
All
E
Clone 1
Clone 2
Clone 3
Clone 4
logFC
pHF
0 1 2 3
CNVs number
CNV state NEU DEL AMP
F
IgM level (mg/dL)
Tumor burden (%)
IgM value
Baseline
PR
Tumor burden
Tumor clone (%)
*FDR<0.05
Tumor clone
1
2
3
4
Baseline C6 C12 C24 C36
Follow-up cycles
G
Tumor clone Clone 1 Clone 2 Clone 3 Clone 4
Tumor cluster C0 C1 C2
Proportion (%)
Patient
Treatment cycle
Response
Responder
Pattern
Patient
W001 W002 W003 W004 W005 W006
W007 W008 W009 W010 W011 W012
W013 W014 W015 W016 W017
Treatment cycle
Baseline C24
C6 C36
C12 C48
Response
VGPR SD
PR PD
MR
Responder
Yes
No
Evolutionary pattern
Devolution
Evolution
No-evolution
*FDR<0.05

Figure 3

Fig. 3

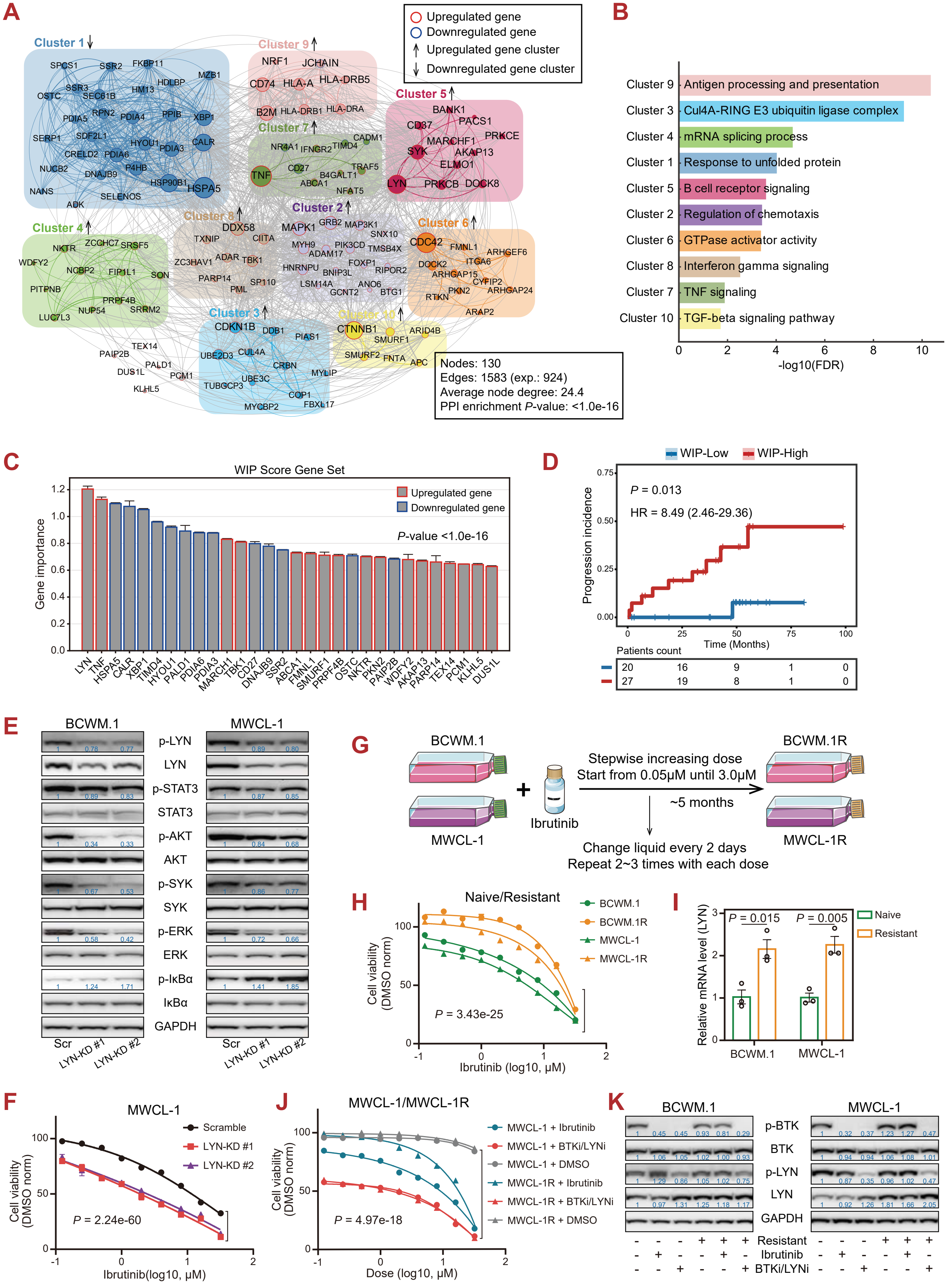

Fig. 4

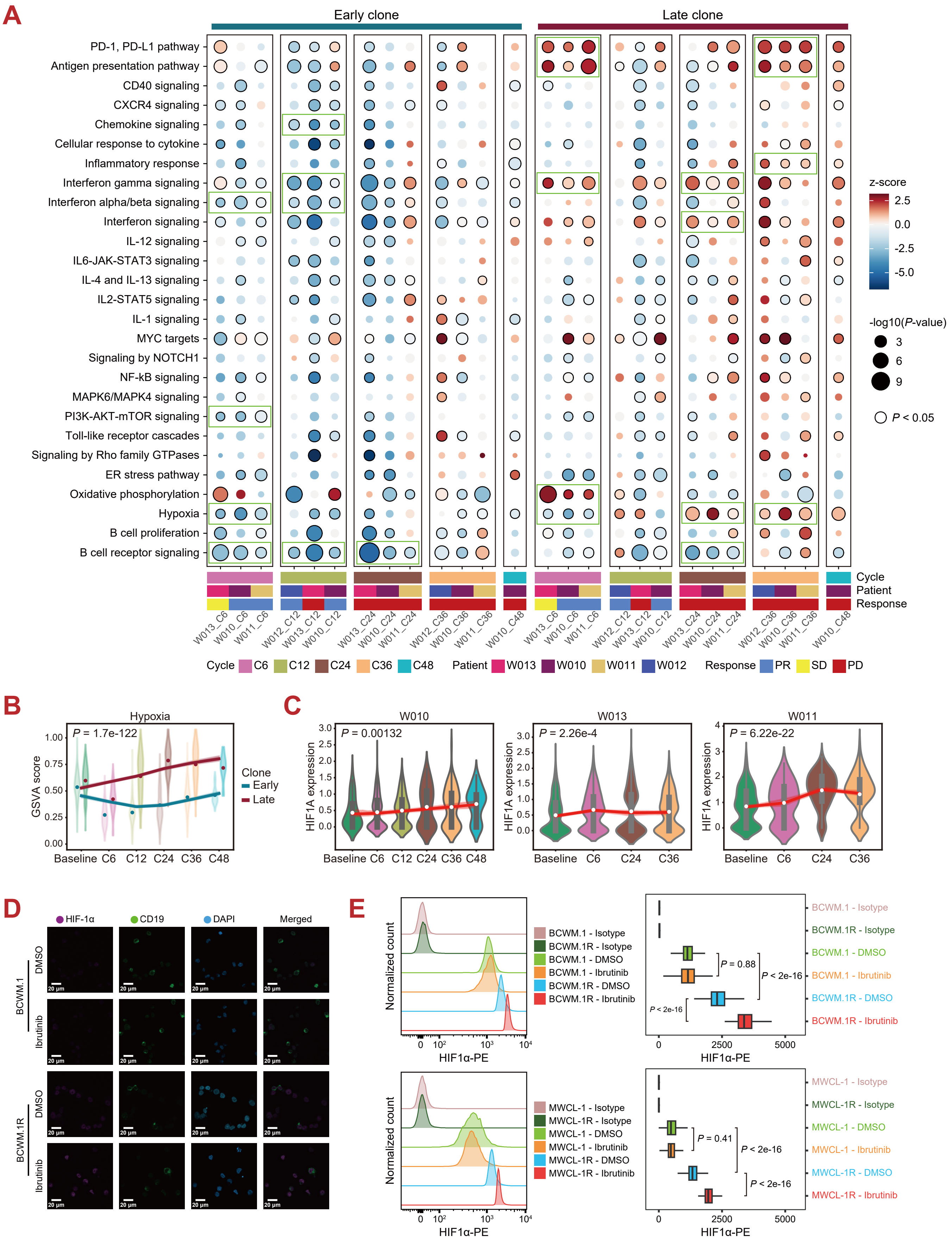
A
Early clone
Late clone
PD-1, PD-L1 pathway
Antigen presentation pathway
CD40 signaling
CXCR4 signaling
Chemokine signaling
Cellular response to cytokine
Inflammatory response
Interferon gamma signaling
Interferon alpha/beta signaling
Interferon signaling
IL-12 signaling
IL6-JAK-STAT3 signaling
IL-4 and IL-13 signaling
IL2-STAT5 signaling
IL-1 signaling
MYC targets
Signaling by NOTCH1
NF-kB signaling
MAPK6/MAPK4 signaling
PI3K-AKT-mTOR signaling
Toll-like receptor cascades
Signaling by Rho family GTPases
ER stress pathway
Oxidative phosphorylation
Hypoxia
B cell proliferation
B cell receptor signaling
z-score
2.5
0.0
-2.5
-5.0
-log10(P-value)
3
6
9
P < 0.05
Cycle
Patient
Response
W013_C6
W010_C6
W011_C6
W012_C12
W013_C12
W010_C12
W013_C24
W010_C24
W011_C24
W012_C36
W010_C36
W011_C36
W010_C48
W013_C6
W010_C6
W011_C6
W012_C12
W013_C12
W010_C12
W013_C24
W010_C24
W011_C24
W012_C36
W010_C36
W011_C36
W010_C48
Cycle C6 C12 C24 C36 C48
Patient W013 W010 W011 W012
Response PR SD PD
B
Hypoxia
P = 1.7e-122
GSVA score
1.00
0.75
0.50
0.25
0.00
Baseline C6 C12 C24 C36 C48
Clone
Early
Late
C
W010
P = 0.00132
HIF1A expression
3.0
2.5
2.0
1.5
1.0
0.5
0.0
Baseline C6 C12 C24 C36 C48
W013
P = 2.26e-4
3.0
2.5
2.0
1.5
1.0
0.5
0.0
Baseline C6 C24 C36
W011
P = 6.22e-22
4
3
2
1
0
Baseline C6 C24 C36
D
HIF-1α
CD19
DAPI
Merged
BCWM.1
DMSO
Ibrutinib
BCWM.1R
DMSO
Ibrutinib
20 μm
E
Normalized count
0
10²
10³
10⁴
HIF1α-PE
BCWM.1 - Isotype
BCWM.1R - Isotype
BCWM.1 - DMSO
BCWM.1 - Ibrutinib
BCWM.1R - DMSO
BCWM.1R - Ibrutinib
P = 0.88
P < 2e-16
P < 2e-16
0
2500
5000
HIF1α-PE
MWCL-1 - Isotype
MWCL-1R - Isotype
MWCL-1 - DMSO
MWCL-1 - Ibrutinib
MWCL-1R - DMSO
MWCL-1R - Ibrutinib
P = 0.41
P < 2e-16
P < 2e-16

Figure 5

Fig 5

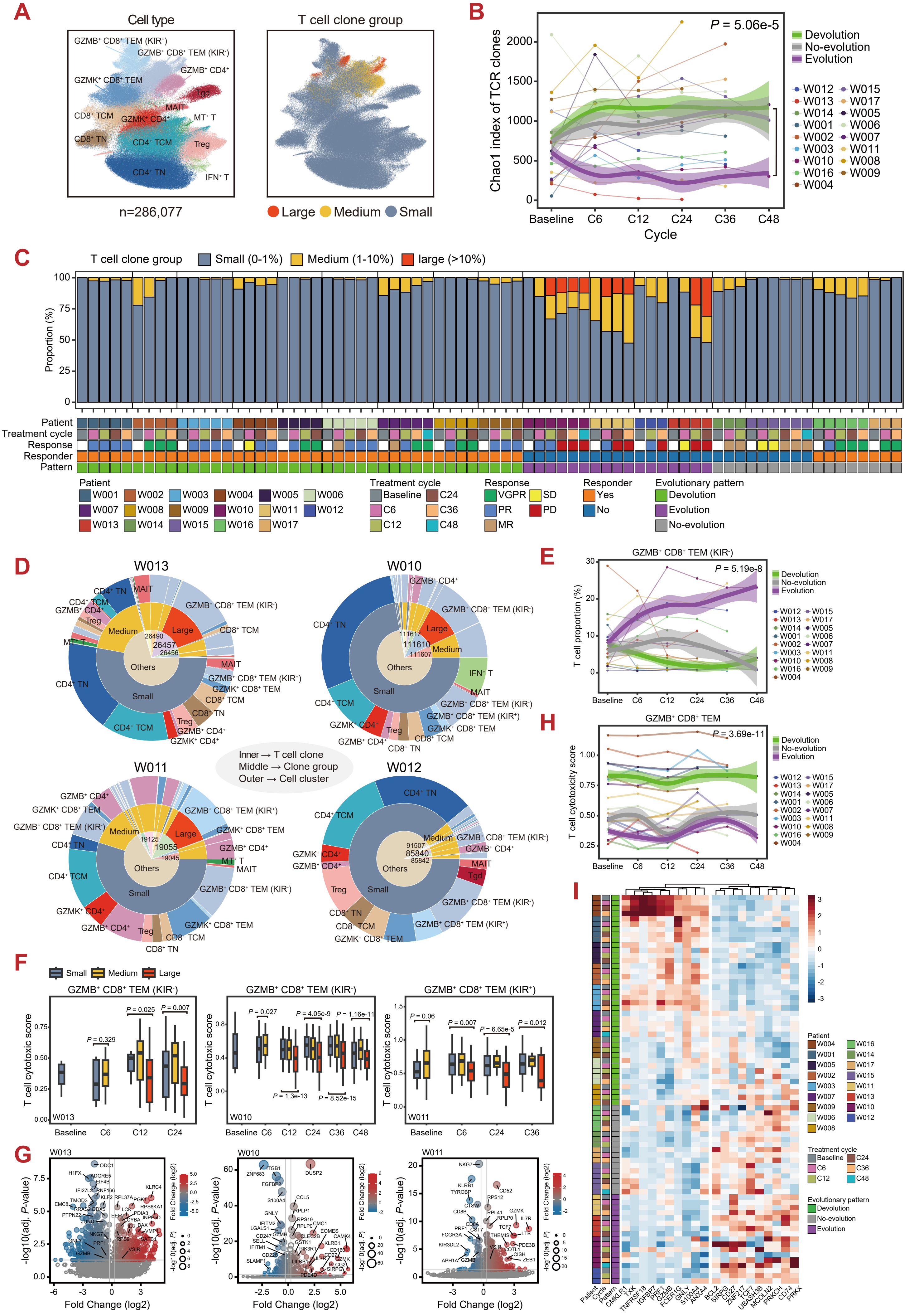

Figure 6

Fig. 6